

# SOLAR ECLIPSE-INDUCED PERTURBATIONS AT MID-LATITUDE DURING THE 21 AUGUST 2017 EVENT

Bolarinwa J. Adekoya<sup>1</sup>, Babatunde O. Adebesein<sup>2</sup>, Timothy W. David<sup>1</sup>, Stephen O. Ikubanni<sup>2</sup>, Shola J. Adebisi<sup>2</sup>, Olawale. S. Bolaji<sup>3,4</sup> and Victor. U. Chukwuma<sup>1</sup>

<sup>1</sup>Department of Physics, Olabisi Onabanjo University, P.M.B. 2002, Ago Iwoye, Nigeria

<sup>2</sup>Space Weather Group, Department of Physical Sciences, Landmark University, P.M.B 1001, Omu-Aran, Kwara State, Nigeria

<sup>3</sup>Department of Physics, University of Lagos, Akoka – Yaba, Lagos, Nigeria

<sup>4</sup>Department of Physics, University of Tasmania, Hobart, Australia

Correspondence to: Bolarinwa J. Adekoya ([adekoyabolrinwa@yahoo.com](mailto:adekoyabolrinwa@yahoo.com); [adekoya.bolarinwa@oouagoiwoye.edu.ng](mailto:adekoya.bolarinwa@oouagoiwoye.edu.ng))

## Abstract

A study of the response of some ionospheric parameters and their relationship in describing the behaviour of ionospheric mechanisms during the solar eclipse of 21 August 2017 is presented. Mid-latitude stations located along the eclipse path and with data availability on the Global Ionospheric radio Observatory (GIRO) database were selected. The percentage of obscuration at these stations range between 63-100%. Decrease in electron density during the eclipse is attributed to reduction in solar radiation and natural gas heating. The maximum magnitude of the eclipse coincided with  $hmF2$  increase and with a lagged maximum decrease in  $NmF2$  consistently at the stations investigated. The results revealed that the horizontal neutral wind flow is as a consequence of the changes in the thermospheric and diffusion processes. The unusual increase/decrease in the shape/thickness parameters during the eclipse period relative to the control days points to the perturbation caused by the solar eclipse. The relationship of the bottomside ionosphere and the F2 layer parameters with respect to the scale height are shown in the present work as viable parameters for probing the topside ionosphere during eclipse. Furthermore, this study shows that in addition to traditional ways of analysing the thermospheric composition and neutral wind flow, proper relation of standardized  $NmF2$  and  $hmF2$  can be conveniently used to describe the mechanisms.

**Keywords:** solar eclipse; solar radiation; bottomside profile parameters;  $NmF2$  and  $hmF2$ ; Topside ionosphere; GIRO database.

## 1 Introduction

Solar eclipse provides opportunity to study the causes of drastic changes in the atmosphere arising from reduction in solar radiation and plasma flux. The atmosphere responded to these changes by modifying the electrodynamic processes and ionization supply of its species to the nighttime-like characteristics during the daytime. Different physical mechanisms (e.g. neutral wind, thermospheric composition, diffusion process etc.) that explain the distribution of plasma at the different ionospheric layers are well established. However, these mechanisms do compete with themselves in explaining the ionosphere, especially the topside ionosphere (see Gulyaeva, 2011).

42 At mid-latitudes, the effect of diffusion processes and its relationship with the thermospheric compositions  
43 has been extensively studied during episodes of solar eclipse (Muller-Wodarg et al., 1998; Jakowski et al.,  
44 2008; Le et al., 2009; Wang et al., 2010; Chuo, 2013). At equatorial and low-latitude regions, the  $E \times B$   
45 plasma drift had been used to explain the circumstances of solar eclipse on transport processes (Adeniyi et  
46 al., 2007; Adekoya et al., 2015). Recently, attention has been drawn to the study of the topside ionosphere  
47 during an eclipse for improved prediction and modelling (Huba and Drob, 2017; Chrniak and Zakharenkova,  
48 2018). Reinisch et al., (2018) compared the modelled and measured studies of electron densities at the  
49 altitude range of about 150 - 400 km during the eclipse. They found that at lower altitude (at about 150 km)  
50 the modelled and the measured agreed well to the changes in the altitude profile of electron density  
51 compared to at higher altitudes. The authors however posited that it would be improved if the model  
52  $NmF2$  peak falls more slowly to better match the data. Consequently, the present study investigates the  
53 effects of solar eclipse of August 21, 2017 on the constituents of the ionosphere at mid-latitudes using  
54 some ionosonde data (bottomside parameters, scale height (H) estimated from the fitted  $\alpha$ -Chapman layer)  
55 which have not been given much attention in previous works especially in analysing solar eclipse effect.  
56 Using these parameters to analyse the circumstances of solar eclipse at the topside ionosphere and its  
57 plasma distribution mechanisms make this paper significantly different from previous studies. Thus, we  
58 intend to achieve by analysing the ionospheric parameters that controls the distribution of plasma at the  
59 topside and bottomside layers of the F2 region. To shed light on these analysis, section 2 highlights the data  
60 source, methodology, and path of the eclipse. The results and discussion were presented in section 3, while  
61 section 4 presents the summary and concluding remark of the result.

62

## 63 **2 The solar eclipse path and Data source**

64 With regards to the eclipse of 21 August 2017, the totality of the eclipse is visible from within a narrow  
65 corridor that traverses the United States of America. However, in the surrounding areas, which include all  
66 of mainland United States and Canada, the eclipse was partial. From the footprint of the Moon's shadow as  
67 seen from some locations, the eclipse started from around 17:00 UT and ended around 20:00 UT. Figure 1  
68 shows the detail coverage area and circumstances of the solar eclipse. More details of its path can be seen  
69 via NASA – Total solar eclipse of 2017 August 21 (<https://eclipse.gsfc.nasa.gov/>). The details on the local  
70 circumstances of the eclipse, the time of the first, mid and last contact of the eclipse over the ionosphere of  
71 the investigated stations was highlighted in table 1. More details on the total solar eclipse event and its  
72 partiality, the circumstances surrounding its progression and its magnitude of obscuration can be obtained  
73 through the link [http://xjubier.free.fr/en/index\\_en.html](http://xjubier.free.fr/en/index_en.html). The path of the eclipse informed the choice of  
74 stations. The ionospheric data used for this study for the selected mid-latitude stations were obtained from  
75 the Global Ionospheric Radio Observatory (GIRO) networks, <http://giro.uml.edu/> (Reinisch and Galkin 2011)  
76 and manually validate. The calculated daily average of summation  $K_p$ ,  $A_p$  and solar flux indices was

77 obtained from the National Space Science Data Centres (NSSDC's) OMNI database  
78 <https://omniweb.gsfc.nasa.gov/>.

79

### 80 **3 Methods of data analysis**

81 *NmF2* values for both the eclipse and control days were obtained from their corresponding critical  
82 frequencies (*foF2*) using the expression:  $NmF2 = ((foF2)^2 / 80.5) \text{ e/m}^3$ . The control day value is the average  
83 value of the two days before/after the eclipse day (i.e. 6, 12, 24 and 27). These reference days were chosen  
84 such that they have similar geomagnetic, interplanetary and solar properties with the eclipse day. The daily  
85 average value of control days and eclipse day interplanetary index (*Ap* and *Kp*), and solar flux unit index  
86 (*F10.7*) ranges from 8 – 12 nT for *Ap*, 2 – 3 for *Kp* index and 75.6 – 89.1 sfu (1 solar flux unit (sfu) =  $10^{-22}$   
87  $\text{Wm}^{-2} \text{ Hz}^{-1}$ ) for *F10.7*, indicating that geomagnetic and solar activities of these days is unsettled (see  
88 Adekoya et al., 2015 for classification of geomagnetic activity). The typical behaviour of the *NmF2* and  
89 *hmF2* on the eclipse day (i.e. *NmF2e* and *hmF2e*) was compared with that of the control day (*NmF2c* and  
90 *hmF2c*) to observe the changes brought by the short period of loss of photoionization in the ionosphere.  
91 This will measure the direct consequence of the solar radiation disruption (due to the eclipse) on the  
92 ionospheric chemical, transport and thermal processes in the F2 layer. The ionized layer depends majorly  
93 on three parameters, viz: *NmF2*, *hmF2*, and the plasma scale height ( $H_m$ ).

94

95 The GIRO provides access autoscaled values of ionospheric parameters generated by Automatic Real-Time  
96 Ionogram Scaler with True height (ARTIST) algorithm, which is inherent in the UMLCAR-SAO Explorer  
97 (Reinisch and Huang 1983; Galkin et al., 2008; Reinisch and Galkin 2011), facilitates the derivation of  
98 bottomside profiles. From the UMLCAR-SAO Explorer, the manually scaled ionogram with high accuracy are  
99 calculated from the standard true-height inversion program (Reinisch and Huang, 1983; Huang and  
100 Reinisch, 1996). The parameters obtained include the critical frequency (*foF2*, Hz), and its height (*hmF2*,  
101 km) of the F layer and the shape (*B1*), and thickness (*B0*) parameters. Likewise, the scale height ( $H_m$ ) of the  
102 F2 layer is obtained from the bottomside. It is estimated from the fitted  $\alpha$ -Chapman function with a  
103 variable scale height,  $H(h)$ , to the measured bottomside profile  $N(h)$ , which then determined as the  
104 Chapman scale height at *hmF2* (i.e.  $H(h > hmF2) \approx H_m(hmF2)$ ) (Huang and Renisch 2001; Reinisch and  
105 Huang 2001; Reinisch et al., 2004). The topside profile is then related to the scale height at the layer, from  
106 the bottomside profile, represented with  $\alpha$ -Chapman function (Reinisch and Huang, 2001). This is because  
107 the Chapman function described the electron density profile,  $N(h)$  aptly. Also,  $H_m$  provides a linkage  
108 between the bottomside ionosphere and the topside profiles of the F region (Liu et al., 2007). Therefore,  
109  $H_m$  describes the constituents of the ionospheric plasma, which decreases with increasing altitude. The  
110 fitting formulas of  $\alpha$ -Chapman function are provided in equation 1 below.

111

$$N_e = N_m F2 \exp \left\{ \frac{1}{2} [1 - z - \exp(-z)] \right\}; \quad z = \frac{h - hmF2}{H_m} \quad 1$$

112 where all the parameters have their usual meaning.

113

114 However, Xu et al. (2013) and Gulyaeva (2011) related ionospheric F2 - layer scale height,  $H$  to the topside  
115 base scale height,  $H_{sc}$ , given by  $H_{sc} = h_{sc} - hmF2 \approx 3 \times H_m$ ). Where  $h_{sc}$  is the height at which the electron  
116 density of the F2-layer falls by a factor of an exponent, at an upper limit of 400 km altitude (i.e.  $NmF2/e$ )  
117 (see Xu et al., 2013). That is, the region where electron density profile gradient is relatively low. Gulyaeva  
118 (2011) showed theoretically that  $H_{sc}$  increase over  $H_m$  by a factor of approximately three (3) and is a  
119 consequence of the  $Ne/NmF2$  ratio ( $Ne$  – plasma density), which corresponds to  $H_m$  in the Chapman layer.  
120 At altitudes very close to  $hmF2$ , the ratio equals 0.832, while it is 0.368 at altitudes beyond the  $hmF2$ .  
121 Therefore, we adopted the definition of Gulyaeva (2011) for the topside base scale height as the region of  
122 the ionosphere between the F2-peak and 400 km altitude. Summarily, the topside based scale height  
123 ionosphere here is defined as the region between the F2 peak and  $h_{sc}$  or  $3H_m$ . It is thus evident that  $H$  is a  
124 key and essential parameter in the continuity equation for deriving the production rate at different  
125 altitudes, a pointer to the F2 topside electron profiler, as well as a good parameter for evaluating the  
126 transport term (Yonezawa, 1966; Huang and Reinisch, 2001; Reinisch and Huang, 2001; Belehaki et al.,  
127 2006; Reinisch et al., 2004). Consequently, the parameter  $H_m$  can be used as a proxy for observation  
128 relating to the topmost side electron density profile. Furthermore, the division of the topsides and the  
129 bottomside ionosphere may be related to the difference in the effective physical mechanisms in the  
130 regions. Hence, the bottomside parameters  $B1$  and  $B0$  of the ionosphere, as presented in this work, helped  
131 in examining the perturbation of solar eclipse in the bottomside ionospheric F2 layer.

132

#### 133 **4 Results and Discussion**

134 This section presents the temporal evolution of the maximum electron density ( $NmF2$ ), and its  
135 corresponding height ( $hmF2$ ) over the ionosphere at the selected mid-latitude stations along the path of  
136 solar eclipse of 21 August 2017. The control day variation relative to the eclipse day is also presented.  
137 Figure 2 presents the variation of maximum electron density and the corresponding peak height, during  
138 both the eclipse and control days. Figure 3 depicts the variation of scale height and the bottomside  
139 parameters ( $B0$  and  $B1$ ) due to the eclipse by superposing plots for both the eclipse and control days.  
140 Analysis of these parameters during an eclipse event may help in the modelling of the ionospheric profiles  
141 (the topsides and bottomside electron density distribution profile) during the short nighttime-like period of  
142 the day.

143

144 Figure 2a presents the  $NmF2$  and  $hmF2$  variations during the eclipse event and the control day over the  
145 Idaho National Lab; having an obscuration magnitude of 100% around the daytime period. The effect of the  
146 disruption of solar radiation was evident as the  $NmF2$  started decreasing at the first contact of the eclipse  
147 compared to an incessant increase on the control day in Fig. 2ai. The start time or first contact (08:43:31

148 LT), the maximum magnitude period (10:01:53 LT) and the end time or the last contact (11:25:46 LT) of the  
149 eclipse are marked with the vertical lines S, M and E respectively. The decrement in  $NmF2$  during the  
150 eclipse phase was due to reduction in the ionization. This reduction caused changes in the photochemical  
151 and transport process of the atmosphere during the daytime, thus exhibiting nighttime characteristics. It  
152 should be noted that the maximum decrease in  $NmF2$  did not coincide with the maximum magnitude of the  
153 eclipse obscuration, rather with a time lag of few minutes, i.e., 1030 LT. This lag period fell within the  
154 relaxation period over Idaho ionosphere, with  $NmF2$  and  $hmF2$  simultaneously attaining their peak  
155 magnitudes of  $1.67 \text{ e/m}^3$  and  $\sim 239 \text{ km}$ . Hence, the ionosphere returned to its pre-eclipse state. Contrary to  
156 the decrease in the  $NmF2$  amplitude at the recovery phase of the eclipse, the  $hmF2$  increases, attained 239  
157 km peak around 1030 LT and then decreases depicting the eclipse caused morphology.

158

159 The ionosphere over Boulder, Eglin AFB, Austin, Millstone Hill and Point Arguello did not show any contrary  
160 variation to that observed over Idaho during the eclipse event. The decrease and increase in  $NmF2$  and  
161  $hmF2$  after the maximum magnitude are simultaneous. The only exception was that the local time at which  
162 each station observed the effects were different. Their obscuration percentage ranged from 62.5 – 93.37%.  
163 This did not cause any significant change in the way they responded to the reduction in solar heating. The  
164 ionosphere over Boulder experienced the totality of the eclipse with 93.37 % magnitude, which is next to  
165 Idaho (100%) in obscuration, the  $hmF2$  was observed to increase few minutes after the maximum  
166 magnitude of the obscuration. This behaviour is typical for other stations at the eclipse window, but the  
167 time of  $NmF2$  minimum decrease did not always coincides with the  $hmF2$  enhancement after the maximum  
168 obscuration. These observations posit that the minimum rate of electron production does not necessarily  
169 translate to the peak electron density of the molecular gases formed. This is because the electron  
170 concentration depends on the loss rate by dissociative recombination, too.

171

172 At mid-latitudes, the ionospheric F2 plasma distribution is controlled by diffusion processes (Rishbeth  
173 1968). There are two basic mechanisms that define the diffusion process during an eclipse: First is the  
174 coolness brought by the partial removal of photoionization (Müller-Wodarg et al., 1998), which is believed  
175 to instigates the downward diffusion process, and the atmospheric expansion due to the gradual increase  
176 in the temperature after the totality. The downward diffusion process was related to the increase in the  
177 molecular gas ( $\text{N}_2$ ) concentration during the cooling process. However, the aftermath of the coolness was  
178 related to the upward diffusion process. These mechanisms were proxy to the electron density distribution  
179 during the eclipse window. Our analysis suggests that the observed decrease in  $NmF2$  is due to the  
180 downward diffusion flux of the plasma while the increase that followed is by upward diffusion (e.g. Le et al.,  
181 2009; Adekoya and Chukwuma 2016). Several works on eclipse (Müller-Wodarg et al., 1998; Grigorenko et  
182 al., 2008; Adekoya and Chukwuma 2016; Hoque et al., 2016) have shown that it was not just the electron

183 density that is being affected during an eclipse window, but the thermospheric wind as well, since the  
184 thermospheric wind emanating from the ratio of gas species is related to the variation in electron density.  
185 It has been observed that the increase in the mean molecular gas of thermospheric composition decreases  
186 the electron density and vice versa. Le et al. (2010) related the valley of electron density distribution during  
187 the eclipse phases to the contraction/compression and expansion of the atmosphere brought by the  
188 decrease and increase in temperature. Chukwuma and Adekoya (2016) attributed the decrease in the  
189 electron temperature to the downward vertical transport process and the decrease in the cooling process  
190 to the upward vertical transport process.

191

192 Figure 3 describes the variation of  $H_m$ ,  $B1$  and  $BO$  in three columns respectively for all the stations. Looking  
193 at the  $H_m$  plots, one can see that there was a define morphological description of  $H_m$  at the eclipse window.  
194 From the first contact of the eclipse, there was an incessant increase in peak variation that maximized some  
195 minutes after the maximum contact of the eclipse, i.e., about 15 – 45 mins later. Following the peak  
196 magnitude after the maximum contact of the eclipse, the  $H_m$  sharply decreases, reaching the minimum  
197 peak before its rather increase throughout the remaining period of the eclipse second phase. It was further  
198 observed that the minimum decrease in  $NmF2$  amplitude corresponds to increase in  $H_m$  at all stations;  
199 implying the upward lifting of the topside electron to the region of higher altitude at the eclipse window.  
200 Hence, the scale height variation highlights the decrease in electron production and the vertical distance  
201 through which the pressure gradient falls at the topside during the eclipse activity. The observation  
202 illustrates the mutual relationship between the  $NmF2$  and  $H_m$ , which may aid in extrapolating the topside  
203 ionospheric profile (Gulyaeva, 2011). In essence, scale height changes observed during the eclipse window  
204 can be used to explain the pressure gradient, electron density distribution and transport processes. In this  
205 sense, the diffusion coefficients are expressed as ratio of determinants (determinant here refers to the  
206 concentration of species ( $[O]$  and  $[N_2]$ )), with the size of the determinants depending upon both the number  
207 of species in the gas mixture and the level of approximation. Therefore, the increase (decrease) in the scale  
208 height can be used as a proxy for downward (upward) diffusion process at the topside ionosphere.  
209 Consequently, the thermospheric wind, which causes plasma distribution in the topside ionosphere, is  
210 induced by solar radiation. Moreover, the significant changes observed in the scale height variation during  
211 the eclipse window also indicated that transport processes are affected as they are temperature  
212 dependent. Therefore, changes in the thermospheric compositions due to the solar eclipse at the topside  
213 layer will affect the density profiles of the ionosphere.

214

215 It is noteworthy that the increase (decrease) in the scale height decreases (increases) the electron density  
216 during the eclipse window. The sensitivity of electron density to temperature at the topside directly affects  
217 the electron density profile (e.g. Wang et al., 2010); as cooling due to decrease in temperature results in

218 decrease in the electron density via reduced ionization. This indicates that the decrease (increase) in  
219 electron temperature at the topside ionosphere causes the increase (decrease) in the scale height, which is  
220 related to the diffusion and transport processes and subsequently affect the pressure gradient of the  
221 plasma. From plots of  $H_m$  (fig. 3) and  $NmF2$  (fig. 2), it was observed that the minimum decrease in  $NmF2$   
222 corresponded with peak increase in scale height. This implies that the topside ionosphere is more sensitive  
223 (than the bottomside) to any changes in the solar radiation. Thus, the pressure gradients can be analysed in  
224 terms of either the scale height or electron density during solar eclipse.

225

226 From column 2 and 3 of Figure 3, we observed that the measured shape ( $B1$ ) and thickness ( $B0$ ) parameters  
227 of the ionosphere over these stations exhibit significant variations during the eclipse event.  $B1$  responded  
228 with a decrease at the first contact of the eclipse compared to the control day. This decrease was gradual  
229 throughout the eclipse window and followed the variation of solar ionizing radiation. However,  $B0$  variation  
230 differs to that of the  $B1$  observation. The  $B0$  increases from the first contact and reached the maximum  
231 peak few minutes after the maximum obscuration magnitude, which coincided with the minimum decrease  
232 in  $B0$ . Generally, the pattern of the day to day variation of the bottomside parameters was the average  
233 morphology, but the increase in the  $B0$  and the decrease in the  $B1$  parameters during the eclipse period  
234 compared to the control day was a notable one and can be related to the perturbation caused by the solar  
235 eclipse. During the eclipse, the solar radiation was lost; trapped atomic ions  $O^+$  was converted into  
236 molecular ion ( $NO^+$  and  $O_2^+$ ) by charge transfer, owing to the sufficient concentration of molecular gasses  
237 ( $N_2$  and  $O_2$ ) (Rishbeth, 1988). The height of the ionospheric slab indeed increased with reduced width,  
238 which is attributable to compression due to loss of solar heating.

239

240 The behaviour of the ionosphere can be explained during solar eclipse with any of the components that  
241 constitute the topside and the bottomside ionosphere and can be looked at, from the angle of the  
242 percentage of concentration of the components. In this regard, the deviation percentage of  $NmF2$  ( $\delta NmF2$ )  
243 and  $hmF2$  ( $\delta hmF2$ ) during the eclipse day away from the control day were plotted in Figure 4. This is done  
244 to describe the contribution of the thermospheric wind and compositions. Although observing the variation  
245 of  $NmF2$  and  $hmF2$  alone can be used for observing the changes in the behaviour of the thermospheric  
246 compositions and wind flow, if properly analysed, but it is more convenient to describe these mechanisms  
247 by standardizing the original variables used during the event. The normalization effort (with the use of  
248  $\delta NmF2$  and  $\delta hmF2$ ) presents the original variation of  $NmF2$  and  $hmF2$  onto directions which maximize the  
249 variance. Consequently, the result can be used for analyses of any mechanisms that drive the ionospheric  
250 plasma, if properly related.

251

252 The deviation percentage in Figure 4 was defined as the ratio of  $((NmF2e - NmF2c)/NmF2c) \times 100$ . The  
253 same relation is defined for the  $hmF2$  parameter. As earlier pointed out, during eclipse period, neutral  
254 composition becomes the dominant chemical process arising from diffusion activities. The increase in the  
255 neutral composition leads to the increase in the molecular gas concentration and compete with diffusion  
256 process. Hence the deviation percentage discusses the neutral composition changes and delineate how  
257 these changes may affect the electron densities as well as its profiles in the atmosphere during the eclipse.  
258 The respective maximum and minimum peak response of the deviation percentage is attributed to the  
259 enhancement and depletion of  $\delta NmF2$ . One can see from the plots, the deviation percentage started  
260 increasing at the first contact of the eclipse (the first dashed vertical line) and reached the maximum,  
261 appearing few minutes after the maximum magnitude of the eclipse (the second dashed vertical line). This  
262 behaviour is similar to the conditions of the neutral compositions during the eclipse event reported by  
263 Muller-Wodarg et al. (1998).

264  
265 Another important process observed in this study is the neutral wind flow effect. To identify the direction  
266 of the wind, the  $\delta NmF2$  colour legend in the contour plots was used in Figure 4. The negative values  
267 represent a westward wind contribution and the positive values is for the eastward wind. Looking at the  
268 marked eclipse region in the figure, it was revealed that the  $\delta NmF2$  started decreasing from the first  
269 contact of the eclipse, maximized few minutes after the maximum contact mark and, thereafter decreases.  
270 It has been established that at daytime, the peak height of the plasma will be reduced due to lost in  
271 recombination. At nighttime, equatorward neutral wind drives the F2-layer plasma to higher altitudes  
272 where recombination rate is slower. The ionospheric processes during solar eclipse is said to represent a  
273 partial nighttime/sunset ionospheric process (Adekoya et al., 2015; Adekoya and Chukwuma, 2016). Thus,  
274 the F2 plasma behaviour at the eclipse window is induced by the equatorward neutral wind flow. The  
275 neutral wind acts jointly with the plasma flows from the topside ionosphere, resulting in F2 region plasma  
276 density variation. Therefore, the westward/eastward neutral wind flow is related to the  
277 depletion/enhancement in the deviation, which was clearly shown in the marked eclipse region of the  
278 figure. The plots in Figure 3 had established the ionospheric dynamics of diffusion processes, neutral  
279 compositions and the flow of neutral wind caused by the eclipse perturbation, which can invariably reduce  
280 the effectiveness and reliability of radio wave propagation.

281  
282 Relative to the mutual relationship between the topside and bottomside ionosphere, we considered the  
283 linear correlation coefficient ( $R$ ) of  $H_m$  versus  $hmF2$  and  $H$  versus  $BO$  during the eclipse window, In Fig. 5.,  $R$   
284 ranges from (0.80 - 0.90) for  $H_m/hmF2$  relationship, and 0.57-0.89 for the  $H_m/BO$  connection. This good  
285 linear agreement revealed the dependence of  $hmF2$  and  $BO$  on the scale height. Apart from revealing the  
286 dependence between the parameters, the relationship may also provide a convenient way for modelling



287 the topside profile from the knowledge of the bottomside parameter,  $BO$ , during the eclipse period.  
288 Further, fig. 6 illustrates the relationship between the bottomside (continuous line) and the topside  
289 (dashed line) ionosphere over Idaho National Lab during solar eclipse compared to the non-eclipse period.  
290 On the left side was the ionospheric profile during the first contact of the eclipse, the middle and right-side  
291 profiles are during the maximum contact and last contact of the eclipse respectively. The black curve  
292 represents the profile for the eclipse day (August 21) and the red curve is for the one of the selected  
293 reference days, August 27. It is clear from the plots that the ionospheric profiles vary with the solar ionizing  
294 radiation at the eclipse window and shows the suitability of using the bottomside F-region for probing the  
295 topside ionosphere. This behaviour was typical for the ionospheric profiles from other stations along the  
296 path of the eclipse. Also, the strong correlation between  $hmF2$  and  $H_m$  indicates that there may be some  
297 interrelated physical mechanisms controlling the behaviour of the plasma at the topside ionosphere during  
298 solar eclipse. That is,  $hmF2$  is strongly depends on neutral wind flow and explain the state of thermospheric  
299 compositions (e. g. Liu et al., 2006; Fisher et al., 2015). Since all these parameters competes during the  
300 eclipse, one can argue that with the accessibility of one, in place of the other (as a consequence of their  
301 relationship), the prediction and modelling of the ionosphere can be conveniently achieved.

302

## 303 **5 Conclusions**

304 This paper presents the induced perturbation of solar eclipse of 21 August 2017 on the ionospheric F  
305 parameters and how they describe the mechanisms of the ionosphere at mid-latitude. The perturbation  
306 effects and dynamics during a solar eclipse episode using ionospheric F2 parameters ( $NmF2$  and  $hmF2$ ), the  
307 bottomside profile thickness ( $BO$ ) and shape ( $B1$ ) parameters of electron density and the plasma scale  
308 height ( $H_m$ ), which are not often used for eclipse study, were investigated. These parameters represent the  
309 state of the F-region ionosphere. The changes observed during the eclipse phase is related to the reduction  
310 in solar radiation and natural gas heating. The  $NmF2$  minimum was attained around 30 - 45 minutes after  
311 the totality of the eclipse when it decreases to about 65% of its control day. This decrease in  $NmF2$  was  
312 uplifted to the higher altitude where recombinational rate is reduce compared to the non-eclipse day. The  
313 thickness and shape parameters which are often limited to the bottomside F-region were seen as viable  
314 parameters for probing the topside ionosphere, relative to the scale height during the eclipse. Therefore,  
315 their relationship in describing one another is established. The implication is that eclipse-caused  
316 perturbation could have been better explained using some ionosonde parameters. The changes in the  
317 neutral wind flow, thermospheric compositions and diffusion processes found their explanation in the  
318 behaviour of the F region plasma during eclipse. In addition, it can be concluded that the behaviour of  
319  $\delta NmF2$  and  $\delta hmF2$  during eclipse can be conveniently used to describe the mechanisms of thermospheric  
320 composition and wind flow.

321

322 **Acknowledgements**

323 We acknowledge use of global ionospheric Radio Observatory data provided by ULMCAR  
324 (<http://ulcar.uml.edu/DIDBase/>) and the World Data Center for Geomagnetism, Kyoto  
325 (<http://wdc.kugi.kyoto-u.ac.jp/index.html>) for geomagnetic activity data. We thank the management team  
326 of the national Aeronautics and Space Administration (NASA) service (<http://eclipse.gsfc.nasa.gov>) and  
327 [http://xjubier.free.fr/en/site\\_pages/SolarEclipseCalc\\_Diagram.html](http://xjubier.free.fr/en/site_pages/SolarEclipseCalc_Diagram.html) for progression and eclipse local  
328 circumstances information. The authors thank Professor Ljiljana R, Cander and the **anonymous reviewers**  
329 for their constructive corrections and suggestions that tremendously improved the structure and quality of  
330 the paper.

331

332 **References**

333 Adeniyi, J. O., Radicella, S. M., Adimula, I. A., Willoughby, A. A., Oladipo, O. A., and Olawepo, O.: Signature  
334 of the 29 March 2006 eclipse on the ionosphere over an equatorial station, *J. Geophys. Res.*, 112 (A6),  
335 A06314. <http://dx.doi.org/10.1029/2006JA012197>, 2007.

336

337 Adekoya, B. J., Chukwuma, V. U., and Reinisch, B. W.: Ionospheric vertical plasma drift and electron density  
338 response during total solar eclipses at equatorial/low latitude, *J. Geophys. Res.*, 120, 8066-8084.  
339 doi:10.1002/2015JA021557, 2015.

340

341 Adekoya, B. J., and Chukwuma, V. U.: Ionospheric F2 layer responses to total solar eclipses at low- and mid-  
342 latitude, *J. Atmos. Sol. Terr. Phys.*, 138-139, 136-160. <http://dx.doi.org/10.1016/j.jastp.2016.01.006>, 2016.

343

344 Belehaki, A., Marinov, P., Kutiev, I., Jakowski, N., and Stankov, S.: Comparison of the topside ionosphere  
345 scale height determined by topside sounders model and bottomside digisonde profiles, *Adv. Space Res.*,  
346 <http://dx.doi.org/10.1016/j.asr.2005.09.015>, 2006.

347

348 Cherniak, I., and Zakharenkova, I.: Ionospheric Total Electron Content response to the great American solar  
349 eclipse of 21 August 2017, *Geophys. Res. Lett.*, <http://dx.doi.org/10.1002/2017GL075989>, 2018.

350

351 Chukwuma, V. U., and Adekoya, B. J.: The effects of March 20, 2015 solar eclipse on the F2 layer in the mid-  
352 latitude, *Advances in Space Research*, 58, 1720-1731. <http://dx.doi.org/10.1016/j.asr.2016.06.038>, 2016.

353

354 Chuo, Y. J.: Ionospheric effects on the F region during the sunrise for the annular solar eclipse over Taiwan  
355 on 21 May 2012, *Ann. Geophys.*, 31, 1891-1898. doi:10.5194/angeo-31-1891-2013, 2013

356

357 Fisher, D. J., Makela, J. J., Meriwether, J. W., Buriti, R. A., Benkhaldoun, Z., Kaab, M., and Lagheryeb, A.:  
358 Climatologies of nighttime thermospheric winds and temperatures from Fabry-Perot interferometer  
359 measurements: From solar minimum to solar maximum, *J. Geophys. Res.*, 120, 6679-6693,  
360 doi:10.1002/2015JA021170, 2015.

361

362 Galkin, Ivan A. Khmyrov, Grigori M., Reinisch, Bodo W. and McElroy, Jonathan: The SAOXML 5: New Format  
363 for Ionogram-Derived Data, *AIP Conference Proceedings*, 974, 160. <http://dx.doi.org/10.1063/1.2885025>,  
364 2008.

365

366 Grigorenko, E. I., Lyashenko, M. V., and Chernogor, L. F.: Effects of the solar eclipse of March 29, 2006, in  
367 the ionosphere and atmosphere, *Geomagnetism and Aeronomy*, 48 (3), 337-351,  
368 <http://dx.doi.org/10.1134/S0016793208030092>, 2008.

369

370 Gulyaeva T. L.: Storm time behaviour of topside scale height inferred from the ionosphere-plasmasphere  
371 model driven by the F2 layer peak and GPS-TEC observation, *Adv. Space Res.*, 47, 913-920.  
372 doi:10.1016/j.asr.2010.10.025, 2011.

373

374 Hoque, M. M., Wenze, I. D., Jakowski, N., Gerzen, T., Berdermann, J., Wilken, V., Kriegel, M., Sato, H.,  
375 Borries, C., and Minkwitz, D.: Ionospheric response over Europe during the solar eclipse of March 20, 2015,  
376 J. Space Weather Space Clim., 6 (A36). doi: 10.1051/swsc/2016032, 2016.  
377

378 Huba, J. D., and Drob, D.: SAMI3 prediction of the impact of the 21 August 2017 total solar eclipse on the  
379 ionosphere/plasmasphere system, Geophys. Res. Lett., 44, 5928-5935.  
380 <http://dx.doi.org/10.1002/2017GL073549>, 2017.  
381

382 Huang, X. and B. W. Reinisch, B. W.: Vertical electron density profiles from the digisonde network, *Adv.*  
383 *space Res.* 18 (6), (6)121 - (6)129, 1996  
384

385 Huang, X. and B. W. Reinisch, B. W.: Vertical electron content from ionograms in real time, *Radio Sci.*, 36  
386 (2), 335 – 342, 2001.  
387

388 Jakowski, N., Stankov, S. M., Wilken, V., Borries, C., Altadill, D., Chum, J., Buresova, D., Boska, J., Sauli, P.,  
389 Hruska, F. and Cander, Lj. R.: Ionospheric behaviour over Europe during the solar eclipse of 3 October 2005,  
390 J. Atmos. Sol. Terr. Phys., 70, 836-853. <http://dx.doi.org/10.1016/j.jastp.2007.02.016>, 2008.  
391

392 Le, H., Liu, L., Yue, X., Wan, W., and Ning, B.: Latitudinal dependence of the ionospheric response to solar  
393 eclipse, J. Geophys. Res., 114, A07308. <http://dx.doi.org/10.1029/2009JA014072> , 2009.  
394

395 Le, H. Le, Liu, Libo, Ding, Feng, Ren, Zhipeng, Chen, Yiding, Wan, Weixing, Ning, Baiqi, Guirong, Xu, Wang,  
396 Min, Li, Guozhu, Xiong, Bo, Lianhuan, Hu: Observations and modeling of the ionospheric behaviors over the  
397 east Asia zone during the 22 July 2009 solar eclipse. J. Geophys. Res., 115, A10313.  
398 <http://dx.doi.org/10.1029/2010JA015609>, 2010.  
399

400 Liu, L., Wan, W., and Ning B.: A study of the ionogram derived effective scale height around the ionospheric  
401 *hmF2*, *Ann. Geophys.*, 24 (3), 851-860. [www.ann-geophys.net/24/851/2006/](http://www.ann-geophys.net/24/851/2006/) , 2006.  
402 #

403 Liu, L., Le, H., Wan, W., Sulzer, M. P., Lei, J., and Zhang, M. -L.: An analysis of the scale heights in the lower  
404 topside ionosphere based on the Arecibo incoherent scatter radar measurements, J. Geophys. Res., 112,  
405 A06307, <http://dx.doi.org/10.1029/2007JA012250>, 2007.  
406

407 Müller-Wodarg, I. C. F., Aylward, A. D., and Lockwood, M.: Effects of a Mid-Latitude Solar Eclipse on the  
408 Thermosphere and Ionosphere - A Modelling Study, *Geophys. Res. Lett.*, 25(20), 3787-3790, 1998.  
409

410 Reinisch, B. W., Dandenault, P. B., Galkin, I. A., Hamel, R., and Richards R. P.: Investigation of the electron  
411 density variation during the August 21, 2017 Solar Eclipse, *Geophys. Res. Lett.*, doi:  
412 10.1002/2017GL076572, 2018.  
413

414 Reinisch, B. W. and Galkin, I. A.: Global Ionosphere Radio Observatory (GIRO), *Earth Planets Space*, 63 (4),  
415 377-381. <https://doi.org/10.5047/eps.2011.03.001>, 2011.  
416

417 Reinisch, B. W., Huang, X., Belehaki, A., Shi, J., Zhang, M., and Ilma, R.: Modeling the IRI topside profile  
418 using scale heights from ground-based ionosonde measurements, *Adv. Space Res.*, 34 (9), 2026-2031.  
419 <https://doi.org/10.1016/j.asr.2004.06.012>, 2004.  
420

421 Reinisch, B. W., and Huang, X.: Deducing topside profiles and total electron content from bottomside  
422 ionograms, *Adv. Space Res.*, 27 (1), 23-30. [https://doi.org/10.1016/S0273-1177\(00\)00136-8](https://doi.org/10.1016/S0273-1177(00)00136-8), 2001.  
423

424 Reinisch, B. W., and Huang, X.: Automatic calculation of electron density profiles from digital ionograms 3.  
425 Processing of bottomside ionograms, *Radio Science*, 18 (3) 477 – 492, 1983.  
426

427 Rishbeth, H.: Solar eclipses and ionospheric theory. Space Science Review, 8 (4), 543-554.  
428 <https://doi.org/10.1007/BF00175006>, 1968.  
429  
430 Rishbeth, H.: Basic physics of the ionosphere: A tutorial review, Journal of Institute of The Electronics and  
431 Radio Engineers, 58 (6S), S207-S223. doi:10.1049/jiere.1988.0060, 1988.  
432  
433 Xu, T. L., Jin, H. L., Xu, X., Guo, P. Wang, Y. B., Ping, J. S.: Statistical analysis of the ionospheric topside scale  
434 height based on COSMIC RO measurements, J. Atmos. Sol. Terr. Phys., 104, 29 – 38.  
435 <http://dx.doi.org/10.1016/j.jastp.2013.07.012> , 2013.  
436  
437 Wang, X., Berthelier, J. J., and Lebreton, J. P.: Ionosphere variations at 700 km altitude observed by the  
438 DEMETER satellite during the 29 March 2006 solar eclipse, J. Geophys. Res., 115, A11312.  
439 <http://dx.doi.org/10.1029/2010JA015497> , 2010.  
440  
441 Yonezawa, T.: Theory of formation of the ionosphere, Space Science Review, 5 (1), 3-56.  
442 <https://doi.org/10.1007/BF00179214>, 1966  
443  
  
444  
445  
446  
447  
448  
449  
450  
451  
452  
453  
454  
455  
456  
457  
458  
459  
460  
461  
462  
463  
464  
465  
466  
467  
468  
469  
470  
471  
472  
473

474  
475  
476  
477  
478  
479  
480  
481  
482  
483  
484  
485  
486  
487  
488  
489  
490  
491  
492  
493  
494  
495  
496  
497  
498  
499  
500  
501  
502  
503  
504  
505  
506  
507  
508  
509  
510  
511  
512  
513  
514  
515  
516  
517  
518

**Table Caption**

**Table 1:** List of ionosonde station, geographic coordinate, eclipse progression time and percentage of maximum obscuration.

**Figure Captions**

**Figure 1:** The orthographic map showing the coverage area and circumstances of the solar eclipse, and the observatory stations of the total solar eclipse event of August 21, 2017 . The thick blue line region of represents the path of the maximum magnitude of the eclipse and the pale blue lines mark the region of where the partial eclipse is experienced, with the magnitude of partiality.

**Figure 2:** Ionospheric  $NmF2$  and  $hmF2$  variations during the eclipse day (black continuous line) and the control day (dash blue line). The three vertical lines represents the different phases of the eclipse (S - start time of the initial phase, M - the period of the maximum magnitude of the eclipse, and E - the end time of the recovery phase or the last contact of the eclipse progression). The local time of the respective eclipse contact points for each station are given in table 1.

**Figure 3:** The local time variation of the ionospheric scale height and the bottomside ( $B0$  and  $B1$ ). The other features are the same as in Fig. 1.

**Figure 4:** Variation of the deviation percentage of  $NmF2$  ( $\delta NmF2$ ) and  $hmF2$  ( $\delta hmF2$ ) magnitudes for observing the changes in the behaviour of the thermospheric composition and wind flow related to the loss rate during the eclipse phase. The three vertical dashed lines marked the eclipse start time, the time of maximum obscuration and the last contact time of the eclipse (i.e. eclipse phase). Table 1 highlights the local time contact point of the eclipse corresponding the international standard time (IST) eclipse progression. The direction of wind was identify using the  $\delta NmF2$  colour legend, the negative values represents the westward wind direction and the positive values is for the eastward wind.

**Figure 5:** Linear relationship of H versus  $hmF2$  and H versus  $B0$  during the eclipse of 21 August 2017 progression phase.

**Figure 6:** Example of the ionospheric profile at the eclipse window of Idaho National Lab showing the bottomside profile (continuous line) and the modelled topside profile shown as a dashed line. The maximum point of the continuous line is the point in which the peak value of the measured foF2 and hmF2 are obtained. The respective measured values foF2, hmF2 and the corresponding B1, B0, and Hm parameters values are provided in the plot. The black curve represents the profile for the eclipse day (August 21) and the red curve is for the one of the selected reference days, August 27. On the left side, was the profile during the first contact of the eclipse, the middle and the right profiles are for the maximum contact and the last contact of the eclipse respectively.

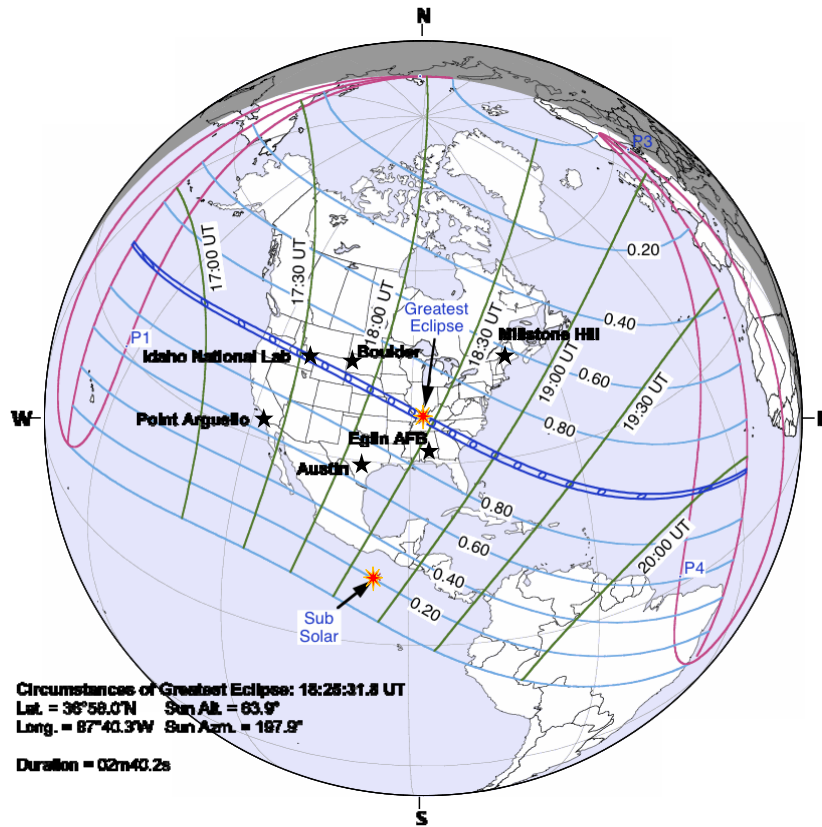
519  
 520  
 521  
 522  
 523  
 524  
 525  
 526  
 527  
 528  
 529  
 530  
 531  
 532  
 533  
 534  
 535

**Table 1:** List of ionosonde station, geographic coordinate, eclipse progression time (Universal time/ Local time) and percentage of maximum obscuration.

Station	GLat	GLong	Eclipse Start time (UT)/(LT)	Eclipse Max Time (UT)/(LT)	Eclipse End Time (UT)/(LT)	% of max obscuration	UT to LT difference
IDAHO NATIONAL LAB	43.81	247.32	16:14:15/ 08:43:31	17:32:37/ 10:01:53	18:56:30/ 11:25:46	100	16:29:17
BOULDER	40	254.7	16:22:33/ 09:21:21	17:46:10/ 10:44:58	19:13:46/ 12:12:34	93.37	16:58:48
EGLIN AFB	30.5	273.5	17:04:41/ 11:18:29	18:37:08/ 12:50:56	20:03:48/ 14:17:36	83.322	18:13:48
AUSTIN	30.4	262.3	16:40:45/ 10:09:55	18:10:10/ 11:39:20	19:39:35/ 13:08:45	65.93	17:29:10
POINT ARGUELLO	34.8	239.5	16:02:39/ 08:00:15	17:16:55/ 09:14:31	18:39:36/ 10:37:12	64.608	15:57:36
MILLSTONE HILL	42.6	288.5	17:27:28/ 12:41:16	18:45:53/ 13:59:41	19:58:38/ 15:12:26	62.533	19:13:48

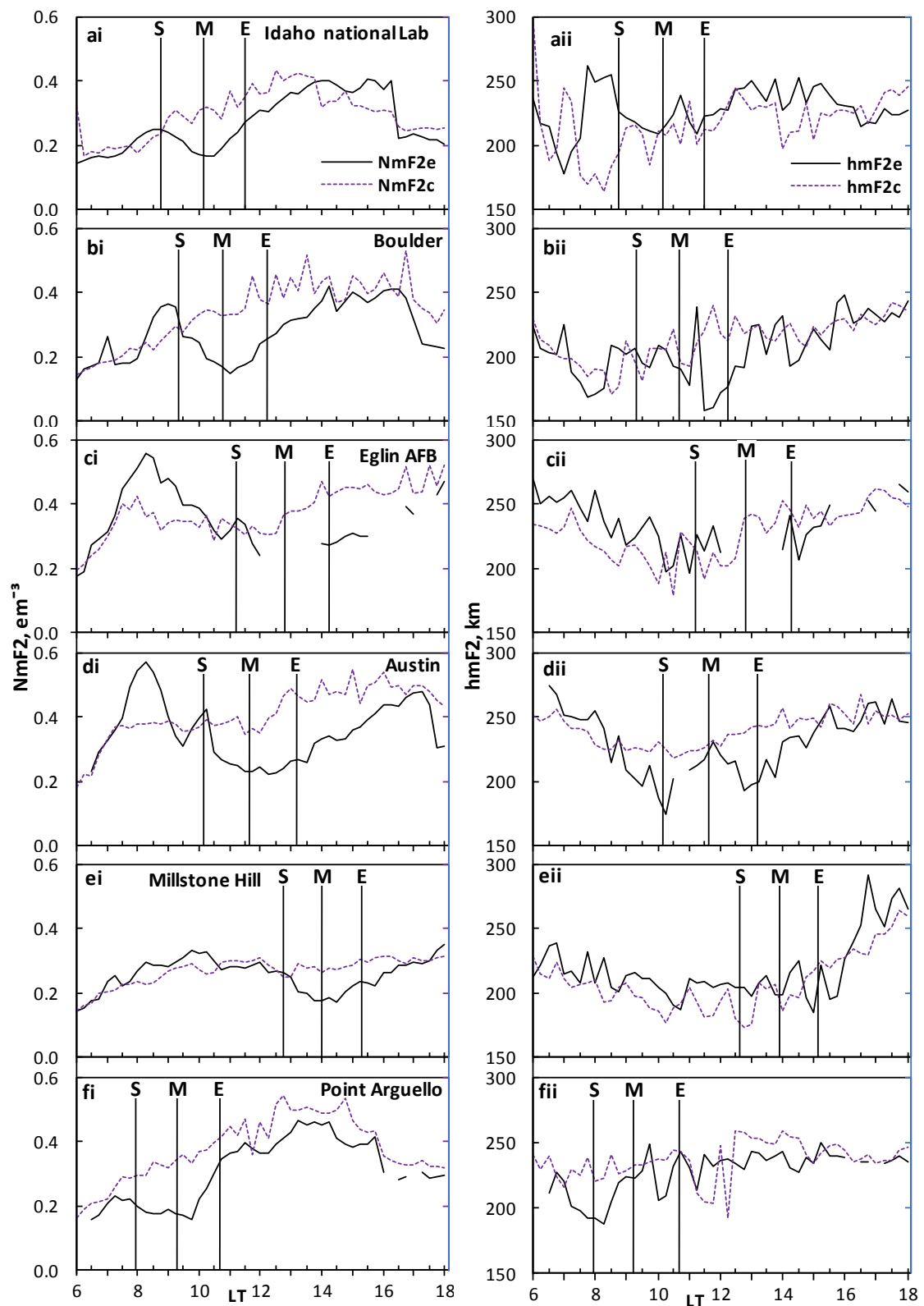
536  
 537  
 538  
 539  
 540  
 541  
 542  
 543  
 544  
 545

546  
547  
548  
549  
550  
551



552  
553  
554  
555  
556  
557  
558

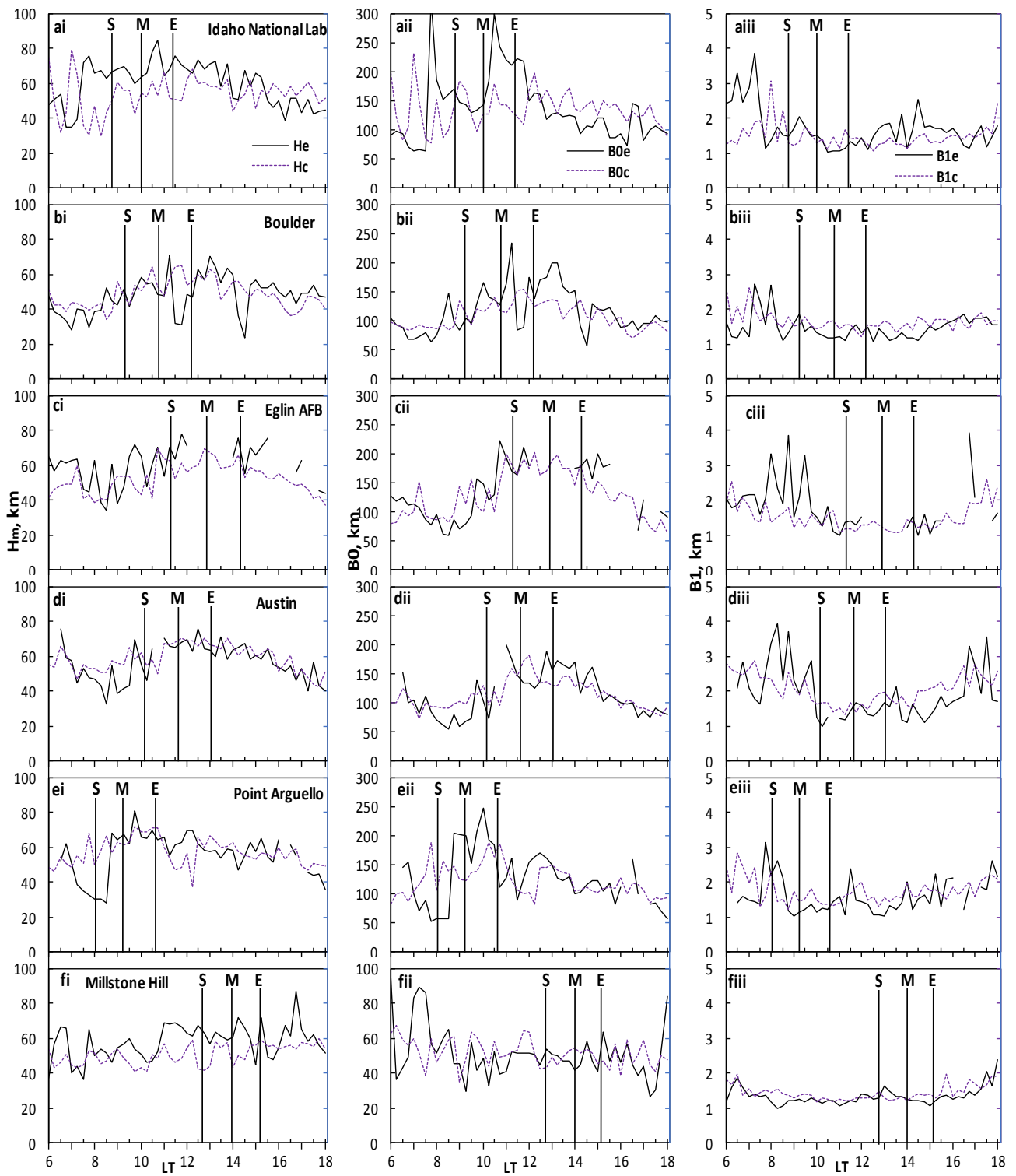
**Figure 1:** The orthographic map showing the coverage area and circumstances of the solar eclipse, and the observatory stations of the total solar eclipse event of August 21, 2017 . The thick blue line region of represents the path of the maximum magnitude of the eclipse and the pale blue lines mark the region of where the partial eclipse is experienced, with the magnitude of partiality.



559

560 **Figure 2:** Ionospheric  $NmF2$  and  $hmF2$  variations during the eclipse day (black continuous line) and the  
 561 control day (dash blue line) was presented to delineate effect of solar eclipse of August 21, 2017 on the  
 562 ionosphere. The three vertical lines represents the different phases of the eclipse (S - start time of the  
 563 initial phase, M - the period of the maximum magnitude of the eclipse, and E - the end time of the recovery  
 564 phase or the last contact of the eclipse progression). The local time of the respective eclipse contact points  
 565 for each station are given in table 1.



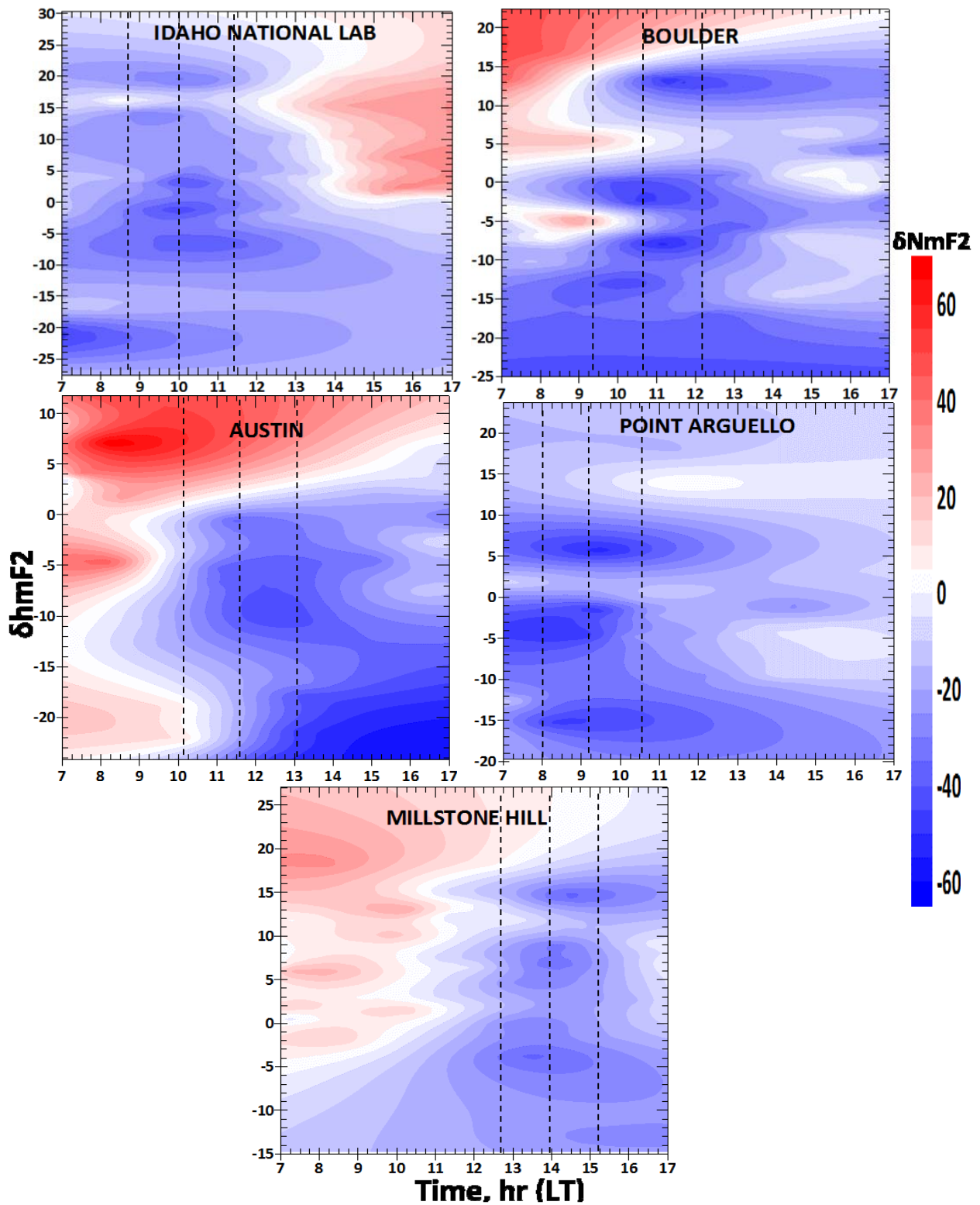


566

567 **Figure 3:** The local time variation of the ionospheric scale height and the bottomside ( $B0$  and  $B1$ ). The other  
 568 features are the same as in Fig. 1.

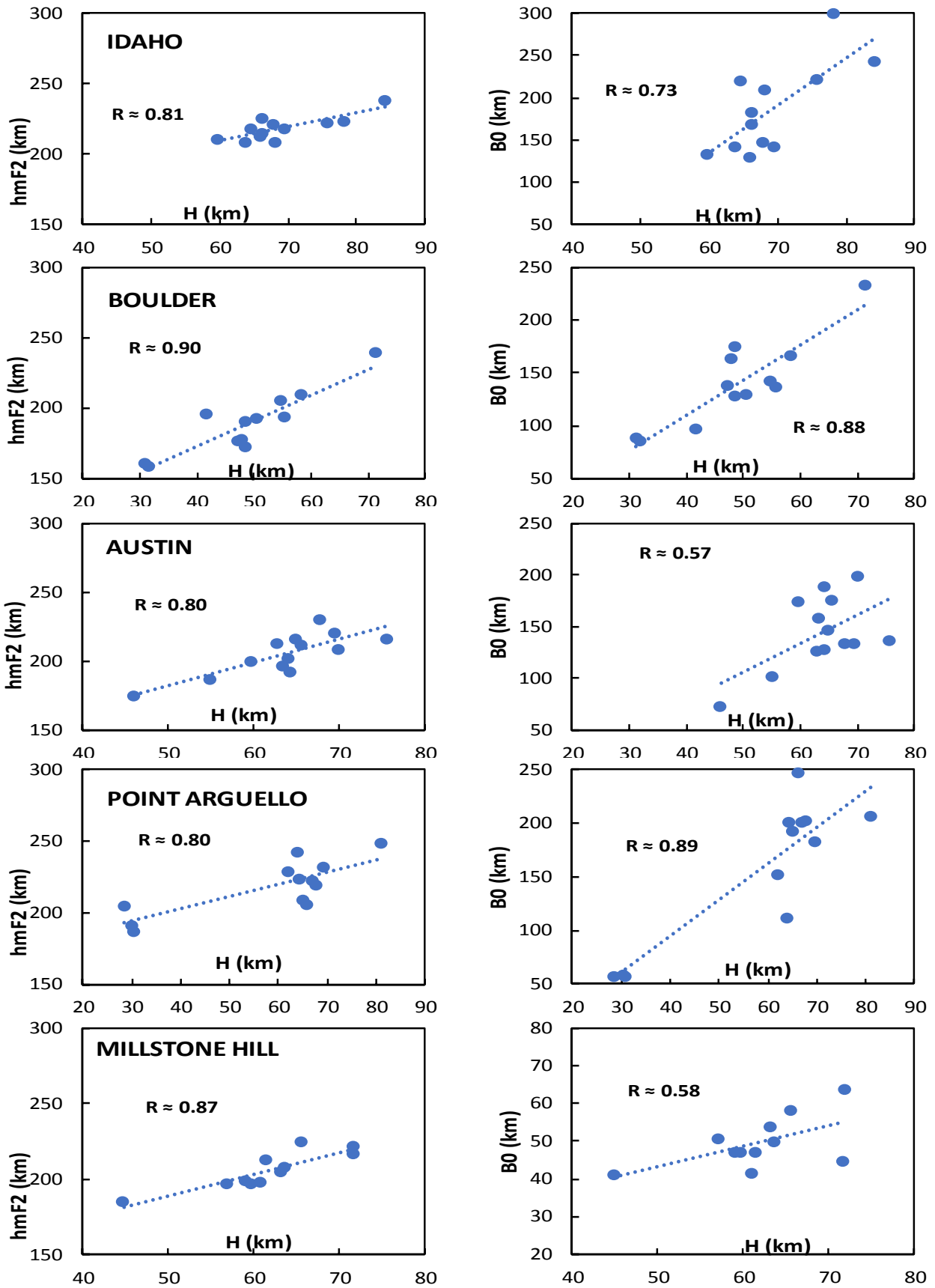
569

570



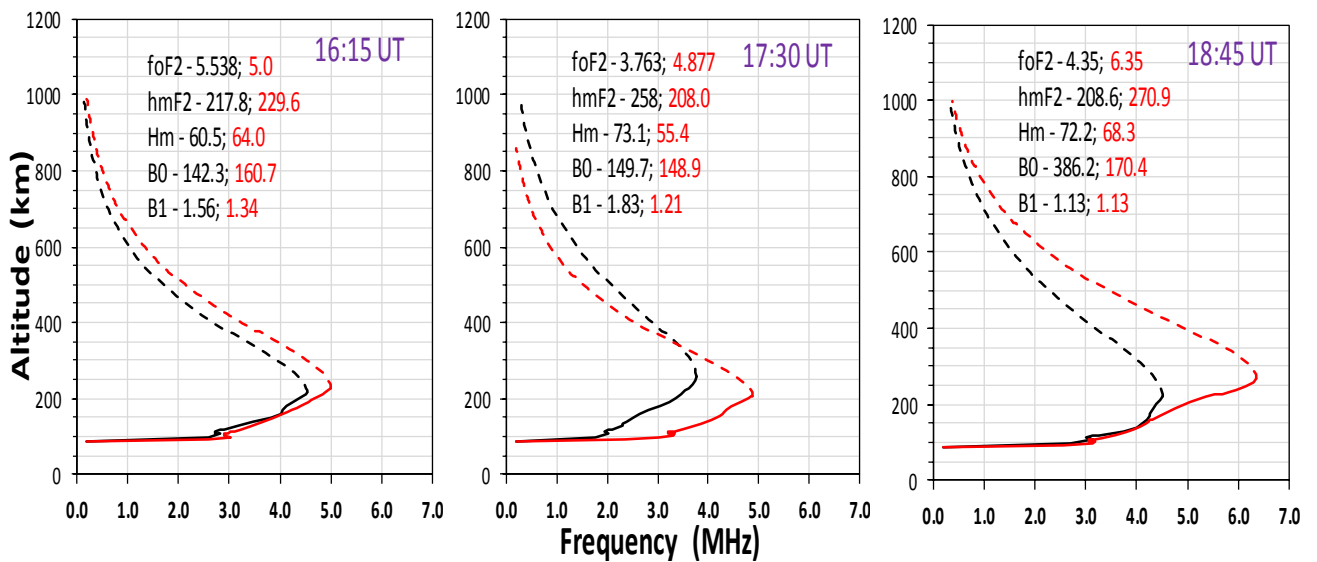
571

572 **Figure 4:** Variation of the deviation percentage of  $NmF2$  ( $\delta NmF2$ ) and  $hmF2$  ( $\delta hmF2$ ) magnitudes for  
 573 observing the changes in the behaviour of the thermospheric composition and wind flow related to the loss  
 574 rate during the eclipse phase. The three vertical dashed lines marked the eclipse start time, the time of  
 575 maximum obscuration and the last contact time of the eclipse (i.e. eclipse phase). Table 1 highlights the  
 576 local time contact point of the eclipse corresponding the international standard time (IST) eclipse  
 577 progression. The direction of wind was identify using the  $\delta NmF2$  colour legend, the negative values  
 578 represents the westward wind direction and the positive values is for the eastward wind.



579

580 **Figure 5:** Linear relationship of H versus *hmF2* and H versus *B0* during the eclipse of 21 August 2017  
 581 progression phase.



582  
 583 **Figure 6:** Example of the ionospheric profile at the eclipse window of Idaho National Lab showing the  
 584 bottomsides profile (continuous line) and the modelled topside profile shown as a dashed line. The  
 585 maximum point of the continuous line is the point in which the peak value of the measured foF2 and hmF2  
 586 are obtained. The respective measured values foF2, hmF2 and the corresponding B1, B0, and Hm  
 587 parameters values are provided in the plot. The black curve represents the profile for the eclipse day  
 588 (August 21) and the red curve is for the one of the selected reference days, August 27. On the left side, was  
 589 the profile during the first contact of the eclipse, the middle and the right profiles are for the maximum  
 590 contact and the last contact of the eclipse respectively.